

Constraints on dark matter annihilation in the Large Magellanic Cloud from multiple low-frequency radio observations

Zhanfang Chen,^{1,2} Feng Huang,^{2,*} and Taotao Fang²

¹*Institute of Modern Physics, Chinese Academy of Sciences, Lanzhou 730000, China*

²*Department of Astronomy, Xiamen University, Xiamen, Fujian 361005, China*

(Dated: December 5, 2024)

Abstract

Low-frequency radio emission from the Large Magellanic Cloud (LMC) is assumed to be dominated by nonthermal synchrotron radiation from energy loss of energetic e^+/e^- in magnetic field. Two different kinds of sources of e^+/e^- , dark matter (DM) annihilation and cosmic rays (CR) related to massive stars, are taken into account in this paper. We fit the multiple low-frequency radio observations, from 19.7 MHz to 1.4 GHz, with a double power-law model $S_{nth} = S_{DM}(\frac{\nu}{\nu_*})^{-\alpha_{DM}} + S_{CR}(\frac{\nu}{\nu_*})^{-\alpha_{CR}}$. ν_* is set to be 1.4 GHz and S_{CR} could be determined from the $24 \mu m$ luminosity based on the global radio-infrared correlation. Our best fit with a fixed α_{CR} changing from 0.80 to 0.55 yields α_{DM} ranging from 0.21 to 0.66. Given a fixed value of α_{CR} , we derive the upper limits of synchrotron emission induced by dark matter annihilation at different radio frequencies. Larger value of α_{CR} represents for a harder e^+/e^- spectrum from cosmic rays, which leads to a smaller value of α_{DM} and allow less synchrotron emission resulted from dark matter annihilation in lower frequency. Under the same assumption on the magnetic field, we find that the lower the frequency, the stronger the restriction on DM parameter space. Meanwhile, as the peak frequency of synchrotron radiation decrease with the energy of e^+/e^- , constraints on DM properties obtained from lower frequency are more severe in the case of DM with lower mass. Future low-frequency radio survey should be considered a promising and powerful way to constrain DM.

* Corresponding author: fenghuang@xmu.edu.cn

I. INTRODUCTION

The particle nature of dark matter remains unclear, indirect detection of dark matter aims to search electromagnetic signals induced by dark matter annihilation in astronomical systems, which could put strong constraints on dark matter mass v.s. annihilation cross section parameter space (m_χ v.s. $\langle\sigma v\rangle$) [1, 2]. In the scenario of the widely discussed dark matter candidate, Weakly Interacting Massive Particles (WIMPs), the final products of self-annihilation include e^+/e^- [3, 4]. Low frequency observations of nearby galaxies have potential to detect the synchrotron radiation from energy loss of such kind of energetic e^+/e^- in magnetic field. Dwarf spheroidal galaxies (dSphs), such as the satellites of our Milk Way, are among the most promising targets to detect dark matter annihilation signal for their deficiency in star formation and then lack of cosmic ray e^+/e^- . Several groups have conducted deep radio observations of the Local Group dSphs with the Australia Telescope Compact Array (ATCA) in the frequency band 1.1 GHz–3.1 GHz [5–8], with the Green Bank Telescope (GBT) at the frequency 1.4 GHz [9, 10]. Very recently, the first observational limits on diffuse synchrotron emission from 14 dSphs at radio frequency below 1.0 GHz have been presented by the combination of survey data from the Murchison Wide field Array (MWA) and the Giant Metre-wave Radio Telescope (GMRT) [11]. Additionally, similar studies have been conducted with data from the TIFR-GMRT sky survey at the frequency 150 MHz for a stacking analysis of 23 dwarf spheroidal galaxies and with FAST data for the Coma Berenices dwarf galaxy [13, 14]. However, no significant detection of a diffuse radio continuum found in these observations. Such a kind of non-detection could also put upper limits on dark matter annihilation, while the limits vary widely due to the large uncertainty of assumed magnetic field and other related astrophysical properties. The nearest dwarf irregular galaxies (dIrrs), the Large Magellanic Cloud (LMC), is also an optimal target for synchrotron radiation searches from dark matter annihilation because of its proximity and its large mass-to-light ratio [15]. Photometric and spectral measurements of LMC have covered almost the entire electromagnetic spectrum, which enables us to deduce properties of magnetic field and star formation. Pioneering radio observations of LMC date back to 1950s [12, 16–18], which include the lowest frequency 19.7 MHz. Recently, For et al. present the first low-frequency MWA radio continuum flux of LMC from the GaLactic Extragalactic All-Sky MWA (GLEAM) survey [19]. In this paper, we aim to revisit the situation of

constraints on dark matter annihilation in LMC with this updated multiple low-frequency radio data included.

Recently, Regis et al. used the Australian Square Kilometer Array Pathfinder (ASKAP) to observe the Large Magellanic Cloud (LMC) at a frequency of 888 MHz [20]. The study did not detect any obvious dark matter signal but was able to provide an upper limit on dark matter annihilation. Tasitsiomi et al. and Chan et al. have utilize radio continuum data from 19.7 MHz to 8.55 GHz to constrain dark matter [21–23]. Tasitsiomi et al. assume synchrotron radiation from dark matter annihilation is proportional to $\nu^{-0.75}$ and the observed flux is regarded as an upper limit induced by dark matter annihilation. A subsequent study has been carried out by Siffert et al., however, they considered constraints from radio emission from 1.4 GHz and 4.8GHz, which may contain large fraction of thermal free–free emission from ionized hydrogen clouds [24]. Furthermore, Chan et al. proposed that the total radio flux consists of two components: non-thermal radiation, primarily contributed by dark matter annihilation and cosmic rays related to massive stars, and thermal radiation [21]. The cosmic ray flux was treated as a free parameter in their fitting process, yet a strong correlation was found between synchrotron emissions from cosmic rays and infrared radiation [25]. In this work, we will focus on radio emission below 1.4 GHz, which is generally believed to be dominated by optically thin synchrotron emission in LMC. We consider the non-thermal radiation obtained by subtracting the thermal radiation component from the total flux, which is attributed to both dark matter annihilation and cosmic rays. We aim to fit the multiple low-frequency radio observations, from 19.7 MHz to 1.4 GHz, with a double power-law model $S_{nth} = S_{DM}(\frac{\nu}{\nu_\star})^{-\alpha_{DM}} + S_{CR}(\frac{\nu}{\nu_\star})^{-\alpha_{CR}}$. ν_\star is set to be 1.4 GHz. Supernova remnants (SNR) are thought to be the main source of cosmic rays and could be deduced from the star formation rate [26]. Synchrotron emission at 1.4 GHz related to cosmic rays, S_{CR} , could be determined from the 24 μm luminosity based on the global radio-infrared correlation[25]. α_{CR} is generally adopted a value around 0.80 [27]. In [19], the best fit of their double power-law model, which accounts for two considered components (thermal and nonthermal), to radio data from 19.7 MHz to 8.55 GHz, yield $\alpha_{CR} = 0.55$. For a fixed value of α_{CR} , we will use the method of Markov Chain Monte-Carlo (MCMC) to fit the data and derive the upper limits of synchrotron emission induced by dark matter annihilation at different radio frequencies.

In this paper, we present revised constrains on dark matter in LMC with updated multiple

low-frequency radio observations included. In Section 2, we fit the multiple low-frequency radio emission with a double power-law model and present the upper limits of synchrotron emission induced by dark matter annihilation at different radio frequencies. In Section 3, we describe our astrophysical model for LMC, including dark matter distribution, magnetic field and properties related to energetic e^+/e^- transportation. We then derive the synchrotron emission induced by dark matter annihilation and constraints on particle parameter space of dark matter. Lastly, we present our conclusions and discussion in Section 4.

A. Radio data

Radio data from 19.7 MHz to 1.4 GHz are taken from Table 2. in [19] as illustrated here in Table I. The study presented the overall radio continuum morphology between 76 MHz and 227 MHz from the GLEAM survey conducted by MWA[19]. The integrated flux densities S_ν in Table 2. in [19] are extracted from $8^\circ \times 8^\circ$ images centred on the LMC. This work alone has added 20 data points below 1 GHz which enable us to do a statistical data fitting.

B. A double power-law model fitting

Previous studies have indicated that the total radio flux S_{tot} is composed of two components: thermal radiation S_{th} and non-thermal radiation S_{nth} [21]. At approximately 1.4 GHz, the thermal radiation S_{th} is measured to be 136.8 Jy, constituting 30 % of the total radio emission [28]. In the optically thin regime, thermal free-free emission from thermal electrons is typically described by $\alpha_{th} = 0.1$ [12]. The thermal flux can be described by the following expression:

$$S_{th} = 136.8 \left(\frac{\nu}{\nu_\star} \right)^{-0.1}, \quad (1)$$

where ν_\star denotes the reference frequency and here we take its value as 1.4 GHz.

We consider two different sources of e^+/e^- contributing non-thermal radiation, namely dark matter (DM) annihilation and cosmic rays associated with massive stars. The internal mechanisms to produce e^+/e^- are quite different and the spectrums of e^+/e^- are not expected to be the same, and so does the synchrotron radiation power law index. Therefore

ν (MHz)	flux (Jy)	reference
19.7	5270 ± 1054	[18]
45	2997 ± 450	[16]
85.5	3689 ± 400	[17]
98.6	2839 ± 600	[17]
158	1736 ± 490	[17]
76	1855.3 ± 315.6	[19]
84	1775.7 ± 302	[19]
92	1574.9 ± 267.9	[19]
99	1451.6 ± 247	[19]
107	1827.6 ± 310.8	[19]
115	1627.5 ± 276.8	[19]
123	1643.3 ± 279.4	[19]
130	1571.8 ± 267.3	[19]
143	1663.7 ± 282.9	[19]
150	1450.1 ± 246.6	[19]
158	1350.4 ± 229.6	[19]
166	1204.3 ± 204.8	[19]
174	1341.4 ± 228.1	[19]
181	1247.1 ± 212.1	[19]
189	1223.9 ± 208.1	[19]
197	1109.8 ± 188.8	[19]
204	1235.3 ± 210.1	[19]
212	1121.6 ± 190.8	[19]
219	1032.4 ± 175.6	[19]
277	1019.7 ± 173.4	[19]
408	925 ± 30	[12]
1400	384 ± 30	[19]
1400	529 ± 30	[12]

TABLE I. Updated multiple low-frequency radio data

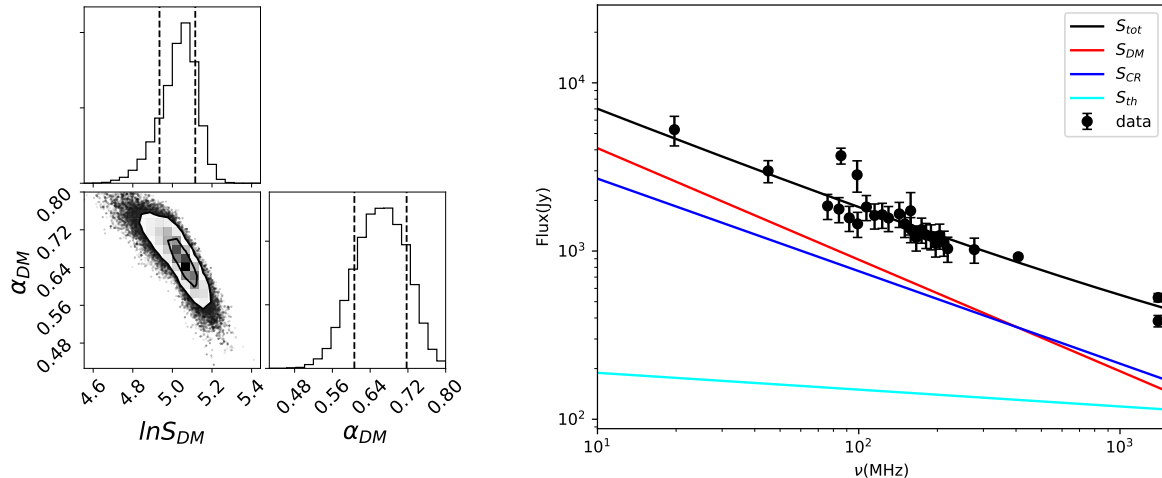


FIG. 1. The left figure shows the contour of the probability distribution of radio flux with two free parameters. The right figure shows the radio flux versus frequency ν . The scatter points represent the observed data listed in Table I. The blue line is synchrotron emission from CRs, the red line represents the allowed upper limit on synchrotron emission related to DM annihilation and the cyan line corresponds to thermal emission. The black line is the sum of these two components. The value of α_{CR} is 0.55.

we utilize a double power-law to fit the data.

$$S_{nth} = S_{DM} \left(\frac{\nu}{\nu_{\star}}\right)^{-\alpha_{DM}} + S_{CR} \left(\frac{\nu}{\nu_{\star}}\right)^{-\alpha_{CR}}, \quad (2)$$

where ν is the radio frequency. S_{DM} (S_{CR}) represents radio flux from dark matter annihilation (cosmic rays) contribution at ν_{\star} and S_{nth} is the non-thermal radiation.

Synchrotron emission from cosmic rays e^{+}/e^{-} has been elaborated intensively in large samples of nearby galaxies. There exists a tight correlation between synchrotron emission and infrared (IR) emission[25]. IR emission is mostly thermal emission from dust that has been heated by the ultra-violet (UV) radiation from young massive stars. These same stars rapidly evolve to supernovae whose remnants are responsible for the production of energetic e^{+}/e^{-} . The empirical relationship between radio and infrared luminosity is:

$$\log \frac{L_{1.4, GHz}}{W \cdot Hz^{-1}} = 1.032 \times \log \frac{L_{24\mu m}}{L_{\odot}} + 11.642 \quad (3)$$

We adopt $S_{24,\mu m} = 8080 \pm 320$ Jy as deduced in [29]. At a distance of 50.1 kpc, $S_{CR}(1.4, GHz) = 177.9 \pm 7.2$ Jy.

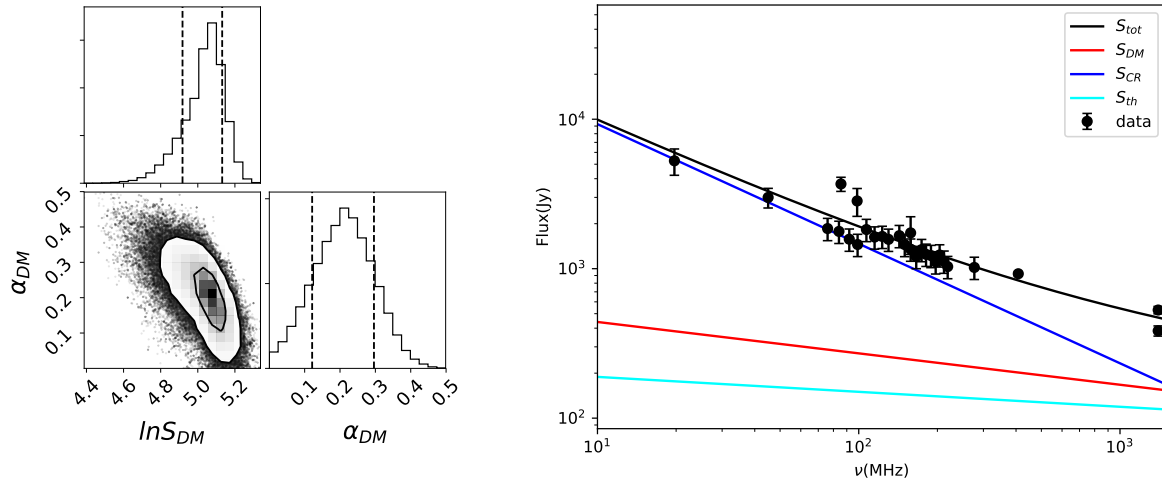


FIG. 2. The left figure shows the contour of the probability distribution of radio flux with two free parameters. The right figure shows the radio flux versus frequency ν . The scatter points represent the observed data listed in Table I. The blue line represents synchrotron emission from CRs, the red line represents the upper limit on synchrotron emission associated with DM annihilation and the cyan line corresponds to thermal emission. The black line is the sum of these two components. The value of α_{CR} is 0.80.

α_{CR} is generally adopted a value around 0.80 [27]. However, for this particular case in LMC, this value is not tightly constrained. In Ref.[19], the best fit to radio data from 19.7 MHz to 8.55 GHz, with both thermal and non-thermal components considered, yields $\alpha_0 = 0.55$ (power law index for the non-thermal component). We will use these two different values of α_{CR} to conduct two different fittings.

Our double power-law model can be rewritten as:

$$S_{nth} = S_{DM} \left(\frac{\nu}{\nu_*} \right)^{-\alpha_{DM}} + 177.9 \left(\frac{\nu}{\nu_*} \right)^{-\alpha_{CR}} \quad (4)$$

For a fixed value of α_{CR} , we will use the method of Markov Chain Monte-Carlo (MCMC) to fit the radio data and derive the upper limits of synchrotron emission induced by dark matter annihilation at different radio frequencies.

We make use of the *emcee* code to do MCMC sampling, which is available online ¹. The script '*Corner.py*' is used for plotting the contours of MCMC samplings [30]. The logarithmic

¹ <https://emcee.readthedocs.io/en/stable/>

likelihood function is defined as:

$$\ln p(S_{nth}|S_{DM}, \alpha_{DM}) = -\frac{1}{2} \sum_{i=1}^N \frac{(S_i - S_{\text{model},i})^2}{\sigma_i^2}, \quad (5)$$

where N is the total number of observational data, S_i is the observed flux in different frequency. $S_{\text{model},i}$ is the theoretical calculation of flux, which is expressed by S_{nth} in Eq.4. Since calculating the theoretical flux is very time-consuming, we calculate the flux under different parameters and obtain the flux of any parameter through interpolation. If dark matter annihilation contribution is set as a fixed value, we can find the total flux corresponding to different α_{DM} values. We further obtain the flux at any set of the two fitting parameters by interpolation.

We present the contours of the probability distribution of flux with two free parameters (α_{DM} and $\ln S_{DM}$) for a given value of α_{CR} in the left panels in Fig.1 and Fig.2. When $\alpha_{CR} = 0.80$, the best fit parameters are $\alpha_{DM} = 0.21^{+0.096}_{-0.091}$ and $\ln S_{DM} = 5.046^{+0.085}_{-0.131}$. When $\alpha_{CR} = 0.55$, the best fit parameters are $\alpha_{DM} = 0.66^{+0.053}_{-0.064}$ and $\ln S_{DM} = 5.038^{+0.074}_{-0.110}$. We then show the two components fit to the multiple low-frequency radio data in LMC in the right panels in Fig.1 and Fig.2. The blue line is synchrotron emission from CRs and the red line represents the allowed upper limit on synchrotron emission related to DM annihilation. The larger value of α_{CR} represents a harder e^+/e^- spectrum from CRs, which leads to a significantly lower allowed synchrotron emission related to DM annihilation when the frequency is less than 300 MHz. Based on the best fits, upper limits on synchrotron emission related to DM annihilation could be written as $155.8(\nu/1.4\text{GHz})^{-0.21}$ for $\alpha_{CR} = 0.80$ and $S_{DM} = 154.5(\nu/1.4\text{GHz})^{-0.66}$ for $\alpha_{CR} = 0.55$. In the next section, we will use this formula to obtain constraints on DM's particle parameter space.

II. CONSTRAINTS ON DARK MATTER PARTICLE PARAMETER SPACE

In the above section, we have deduced synchrotron emission from dark matter annihilation. In order to get the detailed constraints on dark matter particle properties, we firstly need information about the source function of e^+/e^- produced by dark matter annihilation in LMC.

A. e^+/e^- produced from DM annihilation

The source function is the number density distribution of e^+/e^- produced by DM annihilation.

$$q_e(E, r) = \frac{1}{2} \left(\frac{\rho_{DM}(r)}{m_\chi} \right)^2 \langle \sigma v \rangle \frac{dN_e}{dE}, \quad (6)$$

where $\langle \sigma v \rangle$ denotes the velocity averaged annihilation cross section and m_χ is the mass of dark matter particle. dN_e/dE is the electron spectrum of dark matter annihilation, which varies drastically when different annihilation channels assumed. Here we calculate the electron spectrums from different annihilation channels numerically by utilizing DarkSUSY code [31, 32], which is available online ². Fig.3 displays the e^+/e^- spectrum dN_e/dE from four different annihilation channels ($b\bar{b}$, W^+W^- , $\tau^+\tau^-$ and $\mu^+\mu^-$). At the lower energy end, e^+/e^- spectrum from $\tau^+\tau^-$ and $\mu^+\mu^-$ annihilating channel shrinks a lot comparing to that from the other two annihilation channels. Later, we will use $b\bar{b}$ as our benchmark channel while $\mu^+\mu^-$ for comparison.

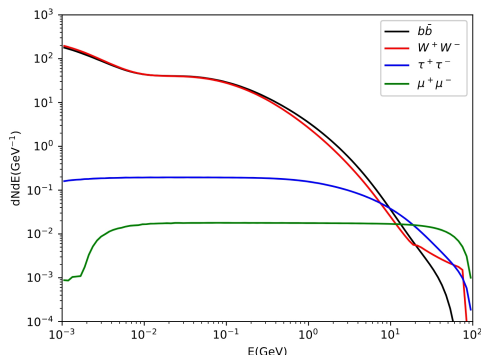


FIG. 3. The e^+/e^- spectrum dN_e/dE from four different annihilation channels: $b\bar{b}$, W^+W^- , $\tau^+\tau^-$ and $\mu^+\mu^-$.

The signal strength resulting from dark matter annihilation is directly proportional to the square of the dark matter density ($\rho_{DM}(r)$). When compared to dwarf spheroidal galaxies, the LMC provides more precise and comprehensive rotational data, facilitating the determination of the dark matter density profiles. However, given our limited understanding of dark matter physics on smaller scales, it is imperative to examine a range of density profiles. In

² <http://www.darksusy.org>

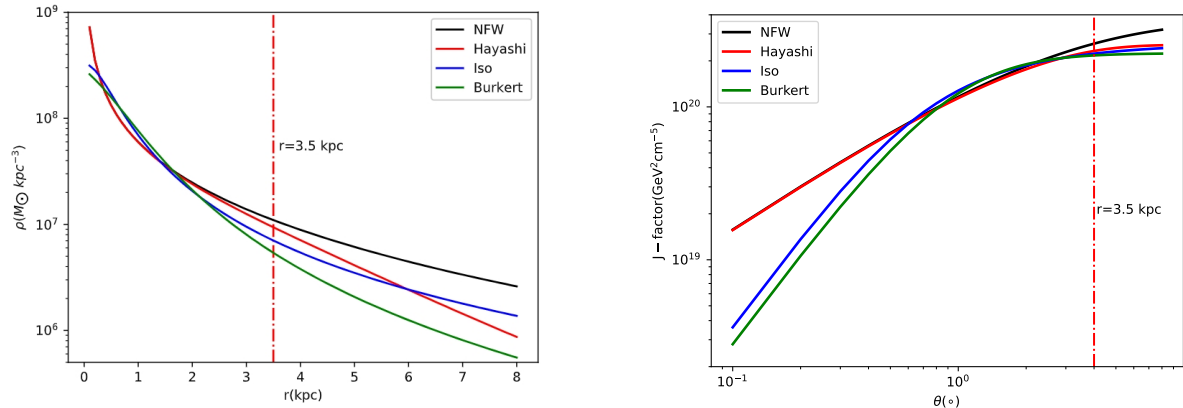


FIG. 4. The left figure depicts the relationship between dark matter distribution and radius, while the right figure illustrates the correlation between the J-factor and the observation angle. We consider four distinct dark matter density profiles: Hayashi (red), NFW (black), Isothermal Sphere (blue), and Burkert (green).

Fig.4 (left), we present the density profiles, including NFW, Hayashi, Isothermal sphere, and Burkert. The associated parameters for these profiles are detailed in Table 2 of the study [24]. Additionally, the J-factor represents a crucial parameter of the dark matter density distribution for regions of interest. The J-factor is computed by integrating the square of the dark matter density ($\rho_{DM}(r)$) along the line of sight while considering the astrophysical characteristics of the region [33]:

$$J = \int \int \rho_{DM}^2(r) dl d\Omega, \quad (7)$$

The right panel of Fig.4 illustrates the values of the J-factor within the 3.5 kpc radius for four density profiles: $2.59 \times 10^{20} \text{ GeV}^2 \text{ cm}^{-5}$ (NFW), $2.32 \times 10^{20} \text{ GeV}^2 \text{ cm}^{-5}$ (Hayashi), $2.23 \times 10^{20} \text{ GeV}^2 \text{ cm}^{-5}$ (isothermal sphere), and $2.17 \times 10^{20} \text{ GeV}^2 \text{ cm}^{-5}$ (Burkert). On the whole, at scales around 3.5 kpc, the density profiles has a negligible impact on the overall flux. Due to the similarity in J-factor values, the NFW profile is predominantly utilized in our subsequent analyses.

B. e^\pm propagation in LMC

Dark matter annihilation injects electrons and positrons in the galaxy halo at a constant rate. The propagation of these charged particles in the tangled magnetic field can be modeled as diffusion. They also lose energy by radiation during this process. As a result, the e^\pm spectrum satisfies the following transport equation [34]:

$$\frac{\partial}{\partial t} \frac{dn_e}{dE_e} = \nabla \left[D(E, \vec{r}) \nabla \frac{dn_e}{dE_e} \right] + \frac{\partial}{\partial E} \left[b(E, \vec{r}) \frac{dn_e}{dE_e} \right] + q_e(E, r), \quad (8)$$

where dn_e/dE_e is the number density of e^\pm per unit energy interval, $D(E, \vec{r})$ is the diffusion coefficient, $b(E, \vec{r}) = dE_e/dt$ represents for the energy loss rate. For simplicity, we assume that D and b are independent of spatial location. The diffusion coefficient $D(E)$ is assumed to have a power law dependence on energy E and magnetic field B :

$$D(E) = D_0 \left(\frac{E}{B_0} \right)^\delta, \quad (9)$$

with δ taken as 0.3, although it is not clear to what extent this relation could be extrapolated. The scale of uniformity for the magnetic field in LMC should be larger than that in dSphs and smaller than that in Milky Way. In this study, we set $B_0 = 2 \mu G$ as our benchmark value. Analyses of the B/C ratio data from the Milky Way suggest that the diffusion coefficient $D_0 = 3 \times 10^{28} \text{ cm}^2 \text{ s}^{-1}$ for the Milky Way with a range from 10^{27} to $10^{29} \text{ cm}^2 \text{ s}^{-1}$ [34, 40, 41]. Given that the gravitational potential well of the LMC is weaker than the Milky Way's, the diffusion coefficient decreases by one to two orders of magnitude. Consequently, we set $D_0 = 3 \times 10^{27} \text{ cm}^2 \text{ s}^{-1}$ as our benchmark values.

The energy loss rate is

$$b(E) = b_{\text{ICS}}(E) + b_{\text{syn}}(E) + b_{\text{ion}}(E), \quad (10)$$

$$b_{\text{ICS}} = 0.76 \frac{U_{ph}}{1 \text{ eV} \cdot \text{cm}^{-3}} \left(\frac{E}{1 \text{ GeV}} \right)^2, \quad (11)$$

$$b_{\text{syn}} = 0.025 \left(\frac{B(\vec{r})}{1 \mu G} \right)^2 \left(\frac{E}{1 \text{ GeV}} \right)^2, \quad (12)$$

$$b_{\text{ion}} = 0.2 \times \frac{N_H}{1 \text{ cm}^{-3}} [\ln(\Gamma) + 6.6], \quad (13)$$

where $N_H \sim 1.3 \times 10^{-6} \text{ cm}^{-3}$ denotes the number density of neutral gas in LMC, β and Γ represent the velocity of e^+/e^- and the Lorentz factor respectively U_{ph} is the total energy

density of the Interstellar Radiation Field (ISRF). We use the fixed value $U_{ph} = 0.539$ eV·cm⁻³, which is the local value of the ISRF in LMC ([35]).

In smaller systems, such as the Milky Way and dwarf spheroidal galaxies, we must take into account the diffusion loss of energetic e^+/e^- [36, 37]. The gravitational potential well and magnetic field strength of the LMC are relatively weaker compared to the Milky Way. When examining smaller systems, such as the LMC, it is essential to take into account the diffusion effect. Ignoring the diffusion loss could result in an incomplete understanding of the underlying physics, potentially leading to incorrect conclusions. Therefore, we must consider the diffusion effect to obtain a more accurate representation of the behavior of energetic e^+/e^- in small systems like the LMC.

In Ref. [34], an analytic solution to Eq.8 has been derived in the case of a spherically symmetric system. Considering the time-independent source and the limit for an electron number density that has already reached equilibrium, the solution takes the form:

$$\frac{dn_e}{dE}(r, E) = \frac{1}{b(E)} \int_E^{M_x} dE' \widehat{G}(r, \Delta v) q_e(r, E') \quad (14)$$

with:

$$\begin{aligned} \widehat{G}(r, \Delta v) = & \frac{1}{[4\pi(\Delta v)]^{1/2}} \sum_{n=-\infty}^{+\infty} (-1)^n \int_0^{r_h} dr' \frac{r'}{r_n} \\ & \times \left[\exp\left(-\frac{(r' - r_n)^2}{4\Delta v}\right) - \exp\left(-\frac{(r' + r_n)^2}{4\Delta v}\right) \right] \\ & \times \frac{\rho^2(r')}{\rho^2(r)}, \end{aligned} \quad (15)$$

where $r_n = (-1)^n r + 2nr_h$ is the location of nth charge image and r_h is the radius of diffusion zone at which a free escape boundary condition is imposed. The value of r_h is generally adopted as twice of the radius of the stellar component. Here in order to compare with observations, we also choose r_h as 3.5 kpc. When \widehat{G} is close to 1 and spatial diffusion can be neglected. In the case of LMC, we need to numerically calculate the integration of the Green Function, which has been presented in Ref.[36] by using the RX-DMFIT code ³. We will follow this process and use RX-DMFIT to deal with diffusion equation.

³ <https://github.com/alex-mcdaniel/RX-DMFIT>

r_h (kpc)	D (kpc)	D_0 (cm^2s^{-1})	B_0 (μG)	ρ_s (GeV/cm^3)	r_s (kpc)	channel
3.5	50.1	3×10^{27}	2.0	0.31	9.04	$b\bar{b}$

TABLE II. Parameters in our benchmark model.

C. Synchrotron emission related to DM annihilation

The synchrotron emission can be approximated as [36]:

$$S_{syn} \approx \frac{1}{D^2} \int_0^{r_{max}} dr r^2 j_{syn}(\nu, r), \quad (16)$$

where $D = 50.1$ kpc is the distance to LMC. The value of r_{max} is set to be 3.5 kpc, which enable the emission region is comparable to $8^\circ \times 8^\circ$ images centred on the LMC. As in Ref.[38], the synchrotron emissivity is

$$j_{syn}(\nu, r) = 2 \int_{m_e}^{M_\chi} dE \frac{dn_e}{dE}(E, r) P_{syn}(\nu, E, r) \quad (17)$$

The average synchrotron power supply in all directions for a certain frequency ν is

$$P_{syn}(\nu, E, r) = \int_0^\pi d\theta \frac{\sin \theta}{2} 2\pi \sqrt{3} r_0 m_e c \nu_0 \sin \theta F\left(\frac{x}{\sin \theta}\right), \quad (18)$$

where $r_0 = e^2/(m_e c^2)$ represents the classical electron radius, θ represents the pitch angle, and $\nu_0 = eB/(2\pi m_e c)$ denotes the non-relativistic gyro-frequency. The x and F quantities are defined follows:

$$x \equiv \frac{2\nu(1+z)m_e^2}{3\nu_0 E^2}, \quad (19)$$

$$F(s) \equiv s \int_s^\infty d\zeta K_{5/3}(\zeta) \approx 1.25 s^{1/3} e^{-s} [648 + s^2]^{1/12}, \quad (20)$$

where $K_{5/3}$ is the modified Bessel function of order 5/3.

D. Constrains on m_χ and $\langle\sigma v\rangle$ parameter space

As illustrated in the above calculation, the synchrotron flux at a given frequency ν is then determined totally by m_χ and $\langle\sigma v\rangle$, which means that the deduced upper limits on synchrotron emission related to DM annihilation at each frequency in last section ν could draw a corresponding upper limit curve in the m_χ and $\langle\sigma v\rangle$ parameter space.

Utilizing deduced upper limit synchrotron emission related DM annihilation ($155.8(\nu/1.4\text{GHz})^{-0.21}$ and $154.5(\nu/1.4\text{GHz})^{-0.66}$), we display constrains on m_χ and $\langle\sigma v\rangle$ parameter space with

two representative frequencies, 19.7 MHz and 1.4 GHz for comparison in Fig.5 and Fig.6. In Table II, we list parameters in our fiducial model and refer to solid lines in Fig.5 and Fig.6. The main feature in these figures is that as the peak frequency of synchrotron radiation decrease with the energy of e^+/e^- , constraints on DM properties obtained from lower frequency are more severe in the case of DM with lower mass. At the same frequency, *eg.* 19.7 MHz, a small value of α_{DM} means a soft energy spectrum resulted from DM annihilation, which leads to less synchrotron emission resulting from dark matter annihilation and in turn presents a stronger constraint on DM parameter space. However, such kinds of constraints are hardly comparable to those obtained from Fermi-LAT gamma-ray[39]. In our benchmark model, all the upper limits are well above the $3 \times 10^{-26} \text{ cm}^3\text{s}^{-1}$, the classical annihilation cross section required for WIMP to make up the dark matter through a thermal production. Numbers of e^+e^- have been significantly reduced in the inner region of the LMC due to diffusion. Deep observation conducted by a low-frequency radio telescope with a large field view will be potential to improve its competitiveness.

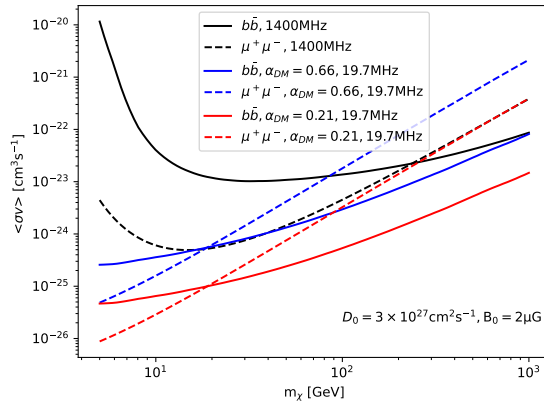


FIG. 5. Constraints on m_χ and $\langle\sigma v\rangle$ parameter space with different annihilation channel for comparison. Solid lines represents the upper limits with $b\bar{b}$. Dashed lines show the upper limits with $\mu^+\mu^-$.

In Fig.5, we add $\mu^+\mu^-$ annihilation channel to compare with $b\bar{b}$ annihilation channel, as shown by the dashed lines. Due to the large shrink of the low energy e^+/e^- spectrum from $\mu^+\mu^-$ annihilating channel, differences between the constraints from different frequencies decrease significantly. Using the $\mu^+\mu^-$ final state as an example, our findings suggest that at $m_\chi = 10 \text{ GeV}$, the value of $\langle\sigma v\rangle$ is limited to $2 \times 10^{-26} \text{ cm}^3 \text{ s}^{-1}$, which is more restrictive

than the constraints obtained by Ref.[24] where $\langle\sigma v\rangle$ is constrained to be around $10^{-25} \text{ cm}^3 \text{ s}^{-1}$ at the same mass range.

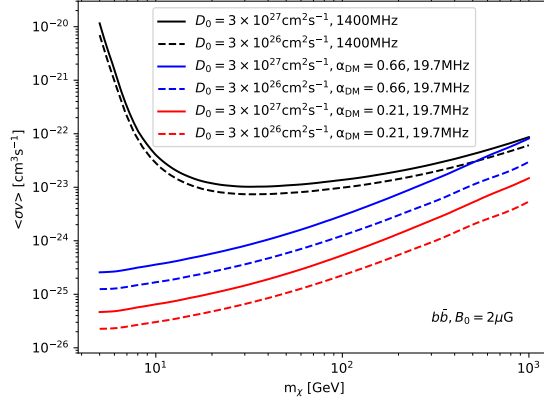


FIG. 6. Constraints on m_χ and $\langle\sigma v\rangle$ parameter space with different annihilation channel for comparison. Solid lines represents the upper limits with $D_0 = 3 \times 10^{27} \text{ cm}^2 \text{ s}^{-1}$. Dashed lines show the upper limits with $D_0 = 3 \times 10^{26} \text{ cm}^2 \text{ s}^{-1}$.

The diffusion coefficient of cosmic ray propagation remains uncertain. Considering that the gravitational potential well of the LMC is weaker than the Milky Way’s, we adopt a benchmark value of $D_0 = 3 \times 10^{27} \text{ cm}^2 \text{ s}^{-1}$. In Fig.6, we compare constraints at $D_0 = 3 \times 10^{26} \text{ cm}^2 \text{ s}^{-1}$ (represented by a dashed line) with those of the benchmark value, suggesting a weaker diffusion process. When D_0 is small, relativistically charged particles with minimal energy loss escape from the diffusion zone. Our findings indicate stronger constraints under weaker diffusion assumptions.

The magnetic field is the most crucial factor in calculating the synchrotron emission[42]. However, the detailed magnetic field distribution in LMC is far from clear. As for the estimated total magnetic field, some studies converge roughly to $6 \mu\text{G}$ ([12, 22]). The maximum value of the total magnetic field is approximately equal to $18.4 \mu\text{G}$. The averaged strength of magnetic field in the inner region could be as high as $5 \mu\text{G}$. Simply for the most conservative limitation, we take the regular magnetic field in the inner region of LMC to be a constant as $\sim 2 \mu\text{G}$ as red solid line shown in Fig.7. We also illustrate the constrains while changing magnetic field strength from $1 \mu\text{G}$ to $10 \mu\text{G}$. It is clear that the deduced upper limits on DM annihilation cross section are sensitive to the assumed magnetic fields.

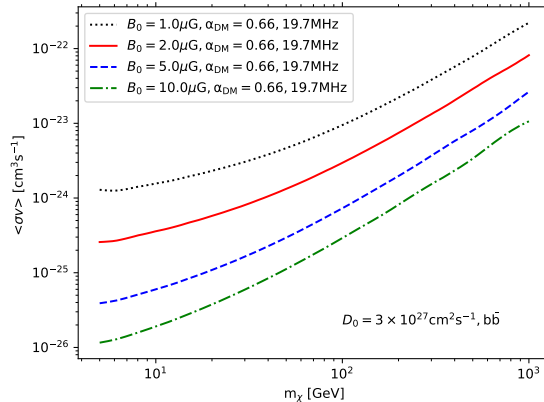


FIG. 7. Constraints on m_χ and $\langle\sigma v\rangle$ parameter space for the strength of magnetic field changing from $1\mu G$ to $10\mu G$

III. SUMMARY

In this paper, we present revised constraints on dark matter particle properties by fitting the updated multiple low-frequency radio observations in LMC. Meanwhile, we take into account two different sources of energetic e^+/e^- , dark matter annihilation and cosmic rays. The latter contribution to low-frequency flux is deduced from the global tight correlation between radio and Infrared luminosity. We find that synchrotron emission from cosmic rays contribution is generally lower than the observed flux in LMC. The spectrum of dark matter annihilation contribution is softer than that of cosmic rays contribution. In this situation, the fraction of dark matter contribution prefers to increase as the frequency increases, which further leads to the lower frequency observations put stronger constraints than that from higher frequency observations. Future extremely low-frequency radio surveys, such as the future low-frequency Square Kilometre Array (SKA) and the proposed radio interferometer array in space, should be considered as a promising and powerful way to constrain dark matter.

IV. ACKNOWLEDGEMENTS

We thank Renyi Ma for his help using emcee code. We thank Hai-kun Li for his support during the preparation for this manuscript. This work was supported by the National

- [1] J. L. Feng, *Ann. Rev. Astron. Astrophys.* **48**, 495-545 (2010) doi:10.1146/annurev-astro-082708-101659 [arXiv:1003.0904 [astro-ph.CO]].
- [2] Porter, T.A., Johnson, R.P., and Graham, P.W.: 2011, *Annual Review of Astronomy and Astrophysics*, 49, 155. doi:10.1146/annurev-astro-081710-102528.
- [3] Bertone G., Hooper D., Silk J. 2005, *Phys. Rept.* 405, 279
- [4] Jungman G., Kamionkowski M., Griest K. 1996, *Phys. Rept.* 267, 195
- [5] M. Regis, L. Richter, S. Colafrancesco, M. Massardi, W. J. G. de Blok, S. Profumo and N. Orford, *Mon. Not. Roy. Astron. Soc.* **448**, no.4, 3731-3746 (2015) doi:10.1093/mnras/stu2747 [arXiv:1407.5479 [astro-ph.GA]].
- [6] M. Regis, L. Richter, S. Colafrancesco, S. Profumo, W. J. G. de Blok and M. Massardi, *Mon. Not. Roy. Astron. Soc.* **448**, no.4, 3747-3765 (2015) doi:10.1093/mnras/stv127 [arXiv:1407.5482 [astro-ph.GA]].
- [7] Regis, M., Colafrancesco, S., Profumo, S., de Blok, W. J. G., Massardi, M., Laura, R., 2014, *JCAP*, 10, 016
- [8] Regis, M., Laura, R., Colafrancesco 2017, *JCAP*, 07, 025
- [9] Spekkens, K., Laura, R., Mason, B. S., Aguirre, J. E., Nhan, B 2013, *Astrophys. J.*, 773, 61
- [10] Natarajan, A., Peterson, J. B., Voytek, T. C., Spekkens, K., Mason, B., Aguirre, J., Willman, B. 2013, *Phys. Rev. D*, 88, 3535
- [11] Kar A., Mitra S., Mukhopadhyaya B., Choudhury, T. R. 2019, *Phys. Rev. D* 100, 043002
- [12] Klein, U., Wielebinski, R., Haynes, R.F., and Malin, D.F.: 1989, *Astronomy and Astrophysics*, 211, 280.
- [13] Basu, A., Roy, N., Choudhuri, S., Datta, K.K., and Sarkar, D.: 2021, *Monthly Notices of the Royal Astronomical Society*, 502, 1605. doi:10.1093/mnras/stab120.
- [14] W. Q. Guo, Y. Li, X. Huang, Y. Z. Ma, G. Beck, Y. Chandola and F. Huang, *Phys. Rev. D* **107**, no.10, 103011 (2023) doi:10.1103/PhysRevD.107.103011 [arXiv:2209.15590 [astro-ph.HE]].
- [15] Sofue, Y.: 1999, *Publications of the Astronomical Society of Japan*, 51, 445. doi:10.1093/pasj/51.4.445.
- [16] Alvarez, H., Aparici, J., and May, J.: 1987, *Astronomy and Astrophysics*, 176, 25.

- [17] Mills, B. Y. 1959, *Handbuch der Physik*, 53, 239
- [18] Shain, C. A. 1959, *URSI Symp. 1: Paris Symposium on Radio Astronomy*, 9, 328
- [19] For, B.-Q., Staveley-Smith, L., Hurley-Walker, N., Franzen, T., Kapińska, A.D., Filipović, M.D., and, ...: 2018, *Monthly Notices of the Royal Astronomical Society*, 480, 2743. doi:10.1093/mnras/sty1960.
- [20] M. Regis, J. Reynoso-Cordova, M. D. Filipović, M. Brüggen, E. Carretti, J. Collier, A. M. Hopkins, E. Lenc, U. Maio and J. R. Marvil, *et al.* *JCAP* **11**, no.11, 046 (2021) doi:10.1088/1475-7516/2021/11/046 [arXiv:2106.08025 [astro-ph.HE]].
- [21] Chan, M. H. & Lee, C. M. 2022, *Astrophys. J.*, 933, 130. doi:10.3847/1538-4357/ac71a9
- [22] Haynes, R.F., Klein, U., Wayte, S.R., Wielebinski, R., Murray, J.D., Bajaja, E., and, ...: 1991, *Astronomy and Astrophysics*, 252, 475.
- [23] Tasitsiomi, A., Gaskins, J., & Olinto, A. V. 2004, *Astroparticle Physics*, 21, 637
- [24] Siffert, B.B., Limone, A., Borriello, E., Longo, G., and Miele, G.: 2011, *Monthly Notices of the Royal Astronomical Society*, 410, 2463. doi:10.1111/j.1365-2966.2010.17613.x.
- [25] Rieke, G. H., Alonso-Herrero, A., Weiner, B. J., et al. 2009, *Astrophys. J.*, 692, 556
- [26] Berezhko, E. G. 2014, *Nuclear Physics B Proceedings Supplements*, 256, 23
- [27] Condon, J. J. 1992, *Annual Review of Astronomy and Astrophysics*, 30, 575
- [28] Hassani, H., Tabatabaei, F., Hughes, A., Chastenet, J., McLeod, A.F., Schinnerer, E., and, ...: 2022, *Monthly Notices of the Royal Astronomical Society*, 510, 11. doi:10.1093/mnras/stab3202.
- [29] Lawton, B., Gordon, K. D., Babler, B., et al. 2010, *Astrophys. J.*, 716, 453
- [30] Foreman-Mackey, D., Vausden, W., Price-Whelan, A., et al. 2016, *Zenodo Software Release*, 2016
- [31] Bringmann T., Edsj J., Gondolo P., Ullio P., Bergstrm L. 2018, *JCAP* 1807, 033
- [32] Gondolo P., Edsj J., Ullio P., Bergstrm L., Schelke M., Baltz E.A. 2004, *JCAP* 07, 008
- [33] V. Bonnivard, C. Combet, M. Daniel, S. Funk, A. Geringer-Sameth, J. A. Hinton, D. Maurin, J. I. Read, S. Sarkar and M. G. Walker, *et al.* *Mon. Not. Roy. Astron. Soc.* **453**, no.1, 849-867 (2015) doi:10.1093/mnras/stv1601 [arXiv:1504.02048 [astro-ph.HE]].
- [34] Colafrancesco, S., Profumo, S. & Ullio, P. 2006, *Astron. Astrophys.* 455, 21
- [35] J. C. Weingartner and B. T. Draine, *Astrophys. J. Suppl.* **134**, 263-282 (2001) doi:10.1086/320852 [arXiv:astro-ph/9907251 [astro-ph]].

- [36] McDaniel, A., Jeltema, T., Profumo, S., & Storm, E. 2017, JCAP, 9, 027
- [37] Cholis, I., Hooper, D., & Linden, T. 2015, Phys. Rev. D, 91, 083507
- [38] Storm, E., Jeltema, T. E., Splettstoesser, M., & Profumo, S. 2017, Astrophys. J., 839, 33
- [39] Ackermann, M., Albert, A., Anderson, B., et al. 2015, Physical Review Letters, 115, 231301
- [40] D. Maurin, F. Donato, R. Taillet and P. Salati, Astrophys. J. **555** (2001), 585-596
doi:10.1086/321496 [arXiv:astro-ph/0101231 [astro-ph]].
- [41] W. R. Webber, M. A. Lee and M. Gupta, Astrophys. J. **390** (1992), 96 doi:10.1086/171262
- [42] Chi, X., & Wolfendale, A. W. 1993, Nature (London), 362, 610